Lab on a Chip

PAPER

View Article Online
View Journal | View Issue

Cite this: *Lab Chip*, 2015, **15**, 1748

GC-on-chip: integrated column and photoionization detector

M. Akbar, H. Shakeel and M. Agah

Received 13th December 2014,
Accepted 4th February 2015

DOI: 10.1039/c4lc01461h

www.rsc.org/loc

This paper reports a unique GC-on-chip module comprising a monolithically integrated semi-packed micro separation column (μSC) and a highly sensitive micro helium discharge photoionization detector (μDPID). While semi-packed μSC with atomic layer deposited (ALD) alumina as a stationary phase provides high separation performance, the μDPID implemented for the first time in a silicon–glass architecture inherits the desirable features of being universal, non-destructive, low power consumption (1.4 mW), and responsive. The integrated chip is 1.5 cm × 3 cm in size and requires a two-mask fabrication process. Monolithic integration alleviates the need for transfer lines between the column and the detector which improves the performance of the individual components with overall reduced fabrication and implementation costs. The chip is capable of operating under the isothermal as well as temperature and flow programming conditions to achieve rapid chromatographic analysis. The chip performance was investigated with two samples: 1) a multi-analyte gas mixture consisting of eight compounds ranging from 98 °C to 174 °C in boiling point and 2) a mixture containing higher alkanes (C_9–C_{12}). Our experiments indicate that the chip is capable of providing rapid chromatographic separation and detection of these compounds (<1 min) through the optimization of flow and temperature programming conditions. The GC-on-chip demonstrated a minimum detection limit of ~10 pg which is on a par with the widely used destructive flame ionization detector (FID).

Introduction

Analysis of volatile organic compounds (VOCs) using gas chromatography (GC) is required for applications in environmental monitoring, homeland security, biomedical diagnostics, and food processing.[1–4] The increasing demand for on-site monitoring of VOCs has led to the development of micro gas chromatography (μGC) systems providing the desirable features of smaller size and higher portability, lower power consumption, and minimal production and maintenance costs. μGCs are realized by employing the micro-electromechanical systems (MEMS) technology which enables the miniaturization of key GC components, namely, preconcentrators,[5–8] separation columns,[9–15] and detectors.[16–18]

Since its first conceptual demonstration by Terry *et al.*,[19] the trend followed by the research community to realize a complete μGC has been the fabrication of individual μGC components and their hybrid integration.[20–25] This implies that the μGC components are assembled manually using fluidic interconnection which is labor intensive, time consuming, prone to error and incompatible with future mass production. Furthermore, each MEMS component in the hybrid approach is designed and developed separately, thereby significantly increasing the fabrication costs. In addition, the presence of cold spots in the fluidic connection between the μGC components mainly "μSC and the detector can adversely affect the column performance. The VOCs after eluting from the μSC may experience extensive band broadening or sample condensation when passing through these cold spots. Thus, there is a critical demand for the development of a monolithic integrated module which includes separation and detection stages on a single chip. Few research milestones accomplished in this regard have been summarized in Table 1.[26–30] The table also describes the features, pros and cons of the monolithic integrated modules. As seen, our group has implemented monolithic integration of polymer-coated open rectangular micro-columns with μTCDs in silicon–glass architectures.[27,28] While being universal and simple to operate, μTCD could not provide very sensitive detection and was sensitive to flow and temperature variations.[31] This restricted the integrated module to operate under flow and temperature programming conditions, and therefore rapid screening of complex mixtures spanning over a wide range of boiling points was not possible. Meanwhile, our group invented the first generation of μDPID in an all-glass

VT MEMS Lab, Bradley Department of Electrical and Computer Engineering, Virginia Tech, Blacksburg, Virginia 24061, USA. E-mail: agah@vt.edu

Table 1 Summary and comparison of the efforts for the monolithic integration of the μSC and detector

References	μSC geometry	Detector type	Pros	Cons
Kaanta (2010)[26]	Microfabricated columns packed with Carbopack/Hayesep A	Thermal conductivity detector	Simple to fabricate, universal	Poor separation efficiency Poor detection limit Sensitive to flow and temperature
Reddy (2012)[29]	Multiple stage microfabricated columns coated with PDMS, Carbowax	Fabry–Perot (FP) cavity sensor	Sub-ng detection limit	Selective Requires laser, photodetector and collimator Bulky and power hungry
Yuz Sun (2010)[30]	1.8 m long regular GC column followed by 10 cm long capillary column	Optofluidic ring resonator (OFRR)	Sub-ng detection limit	Selective Fragile, difficult to operate for field-application
Narayanan (2012)[28]	Microfabricated columns coated with PDMS	Thermal conductivity detector (anchored to the substrate)	Simple to fabricate, universal	Poor detection limit (1 ng) High power consumption (50 mW) Sensitive to flow and temperature
Narayanan (2013)[27]	Microfabricated columns coated with PDMS	Thermal conductivity detector (released in the fluidic channel)	Good detection limit (100 pg)	Complex fabrication procedure Sensitive to flow and temperature

format.[18] In this paper the fabrication of μDPID in a silicon–glass format has been demonstrated which led to the development of a new GC-on-chip module addressing the deficiencies listed in Table 1. The chip comprises a high performance semi-packed μSC with novel stationary phases based on atomic layer deposition and a μDPID. The chip requires only two masks for fabrication. Our comprehensive characterization of the integrated chip indicates that it provides highly efficient separations, reduced analysis times using temperature and flow programming, very sensitive detection equivalent to the current state-of-the-art commercial FIDs, and fast detector response times suitable for high speed gas chromatography.

Chip operation

Fig. 1 shows the conceptual image elaborating the working principle of the chip. The dimensions chosen for the μSC and μDPID in the module are based on our previous work.[11,31] A mixture of VOCs is introduced through the inlet port of the chip which travels through the semi-packed μSC with an inert carrier gas called the mobile phase. The inner surface of the μSC is covered with a finely controllable stationary phase which is a silane-treated alumina layer as established in our previous work.[11] The compounds spend different amounts of time in the stationary phase coating depending on their relative solubility and vapor pressure in the stationary phase, and hence, they emerge from the μSC at different times. This results in their separation into individual compounds. The operation of the new silicon–glass μDPID is similar to that implemented in the glass–glass architecture as described previously.[18] Briefly, a high voltage DC discharge in helium is generated across a pair of excitation electrodes separated by a 20 μm gap. The discharge is sustained by the continuous supply of helium from the auxiliary channel. The discharge is a complex mix of positively and negatively charged ions, metastable He atoms, electrons, and photons (ionizing flux). The photons (energy >10 eV) and metastable He atoms (energy >19.8 eV) are responsible for the ionization of VOCs emerging from the outlet of μSC. The distance of the micro-plasma from the μSC outlet is 1 mm. The outlet of the μSC bypasses the micro-plasma for two purposes: 1) it enables non-destructive analysis and 2) it allows the flow programming of the μSC without significant noise generation in the detector baseline as will be seen later. In addition to the pair of excitation electrodes, the detector is also equipped with a bias and a collector electrode. The bias and the collector electrodes are 1.5 mm apart. The space between the μSC outlet and the collector is called the collector volume. The ionized compound induces a current in the collector electrode. This current is measured by a picoammeter connected to the collector electrode. The purpose of the bias electrode is to collect the negatively charged species from the ionizing flux. This reduces the possibility of their recombination with the ionized compound inside the collector volume which can lead to the reduction in the collector current.

Experimental section

Materials

All test compounds used in this work were purchased from Sigma-Aldrich (St. Louis, MO) in >99% purity. AZ9260 photoresist was purchased from MicroChemicals (Germany) while titanium and gold were purchased from Kurt J. Lesker. Silicon wafers (4 in. diameter, 500 μm thick, n-type, single

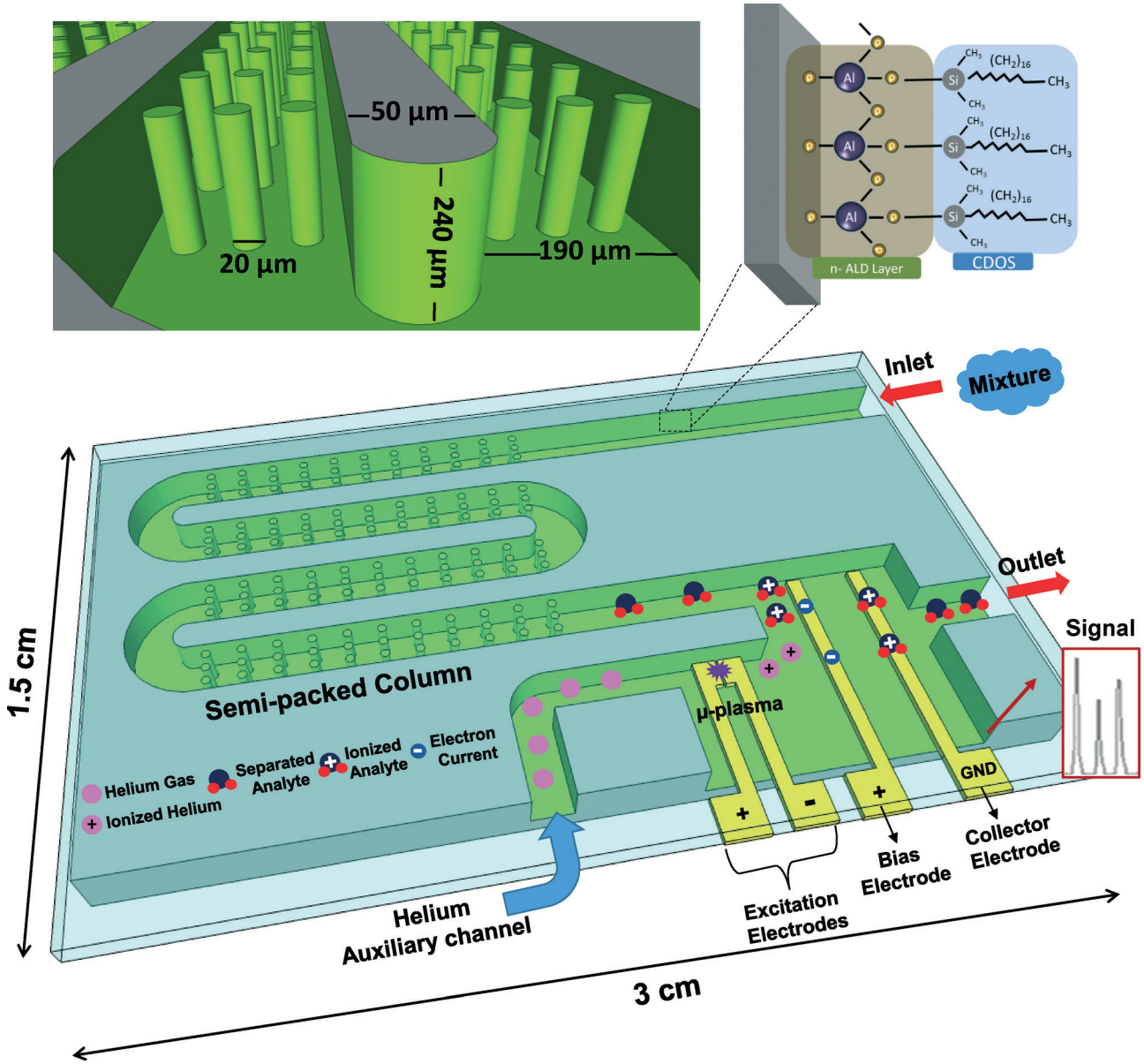

Fig. 1 Conceptual image showing the operation of the monolithic integrated chip (GC-on-chip). The top right image shows the stationary phase coating procedure while the top left image shows the channel dimensions of the micro separation column.

side polished) and borosilicate glass wafers (Borofloat, 4 in. diameter, 700 µm thick, double side polished) were purchased from University Wafers and Coresix Precision Glass (Williamsburg, VA), respectively. Fused capillary tubes (200 µm outer diameter, 100 µm inner diameter,) and Epoxy 907 were purchased from Polymicro Technologies (Phoenix, AZ) and Miller Stephenson (Danbury, CT), respectively. Ultra high purity helium (UHP 300) and industrial grade air (AIB 300) were purchased from Airgas (Christiansburg, VA).

A multicomponent mixture including eight compounds (*n*-heptane, toluene, tetrachloroethylene, chlorobenzene, ethylbenzene, *p*-xylene, *n*-nonane and *n*-decane) was prepared. Equal volumes of 200 µl were pipetted into an autosampler vial for each compound except for *n*-heptane and toluene. Based on the response of both FID and µDPID, a 20 µl volume of each of *n*-heptane and toluene was deemed sufficient to produce peak heights comparable to the other compounds. Another mixture of high-boiling hydrocarbons including *n*-nonane, *n*-decane, *n*-undecane and *n*-dodecane was prepared by pipetting 50 µl, 100 µl, 300 µl and 500 µl volumes of each compound, respectively.

A 5 parts-per-million (ppm) solution of *n*-octane was prepared by pipetting 5 µl of *n*-octane in a custom-made 1 L volumetric flask. The mouth of the flask was sealed with a 24/40 septa and left overnight to allow *n*-octane to volatilize. To prepare a fresh sample again, the *n*-octane in the flask was cleared by heating the flask in an oven set to 80 °C for approximately half an hour followed by purging with nitrogen.

Chip fabrication

The fabrication process for the monolithic chip required two masks: one for the bulk micro-machining of the silicon wafer to create the separation stage, fluidic interconnections and cavities for the detector and the other for the metallization of the Borofloat substrate which served as the detection stage. The silicon wafer processing started with spin coating of the AZ9260 photoresist at 2000 rpm to achieve an ~8 μm thick photoresist layer (Fig. 2a). The wafer was then patterned using a mask aligner (Karl Suss) and developed in AZ400K. The wafer was subjected to a deep reactive ion etcher (DRIE, Alcatel) which resulted in the creation of 190 μm wide and 240 μm deep channels with 20 μm embedded circular micro-pillars and a cavity (Fig. 2b). The photoresist was then stripped off using acetone. Finally, the chip was coated with a thin layer (~10 nm) of alumina deposited at 250 °C using the atomic layer deposition (ALD) technique (Fig. 2c). The lithography step for the fabrication of the detector electrodes on the Borofloat wafer followed the same procedure as described earlier. However, after the development of photoresist the hard-bake time was reduced to 1 min at 110 °C to facilitate the subsequent lift-off process. A 700 nm/40 nm thick Ti/Au metal stack was evaporated using an e-beam evaporator (PVD-250, Kurt J. Lesker) to serve as the detector electrodes. The wafer was left in acetone for 10 min and then placed in a sonic bath for 15 s to ensure complete lift-off (Fig. 2d). Before anodic bonding, both silicon and Borofloat wafers were diced into individual devices. The substrates were aligned and bonded at 1000 V and 370 °C for 45 min (Fig. 2e). After bonding, the edge of the detector cavity was sealed with epoxy and the electrical wires were soldered to the bond pads. Next, the capillary tubes were inserted into the three ports of the chip. Finally, the functionalization of the alumina film and Borofloat cover was accomplished by filling the μSC with 10 mM chlorodimethyloctadecylsilane (CDOS) in toluene for 24 h at room temperature (Fig. 2f). The inlet and outlet of the chip were attached to the injector and the FID of a conventional GC system. The μSC temperature conditioning was performed in the GC oven for approximately 1 h (35 °C ramped at 2 °C min^{-1} to 150 °C) at a constant inlet pressure of 10 psi.

Testing setup

The testing setup for the chromatographic evaluation of the fabricated chip is shown in Fig. 3. A bench-top 7890 series Agilent GC system equipped with two electronic pressure control (ECP) inlets, an FID and an autosampler (7359A) module was used for this purpose. Helium was used as the carrier gas while the injectors and the FID were maintained at 280 °C. The inlet of the chip was connected to injector A while the outlet was fed to the FID for cross-examination purposes. The auxiliary channel of the chip was connected to injector B to provide helium for the micro-plasma generation. The micro-plasma was initiated across a 20 μm gap by applying a 550 V DC voltage using a high voltage power supply (PS-310, Stanford Research Systems) to the excitation electrode pair establishing the baseline current which was recorded on a picoammeter (Model 480, Keithley) connected to the collector electrode. A 100 MΩ resistor (not shown in the Fig. 3) was connected in series with the excitation electrodes to avoid an

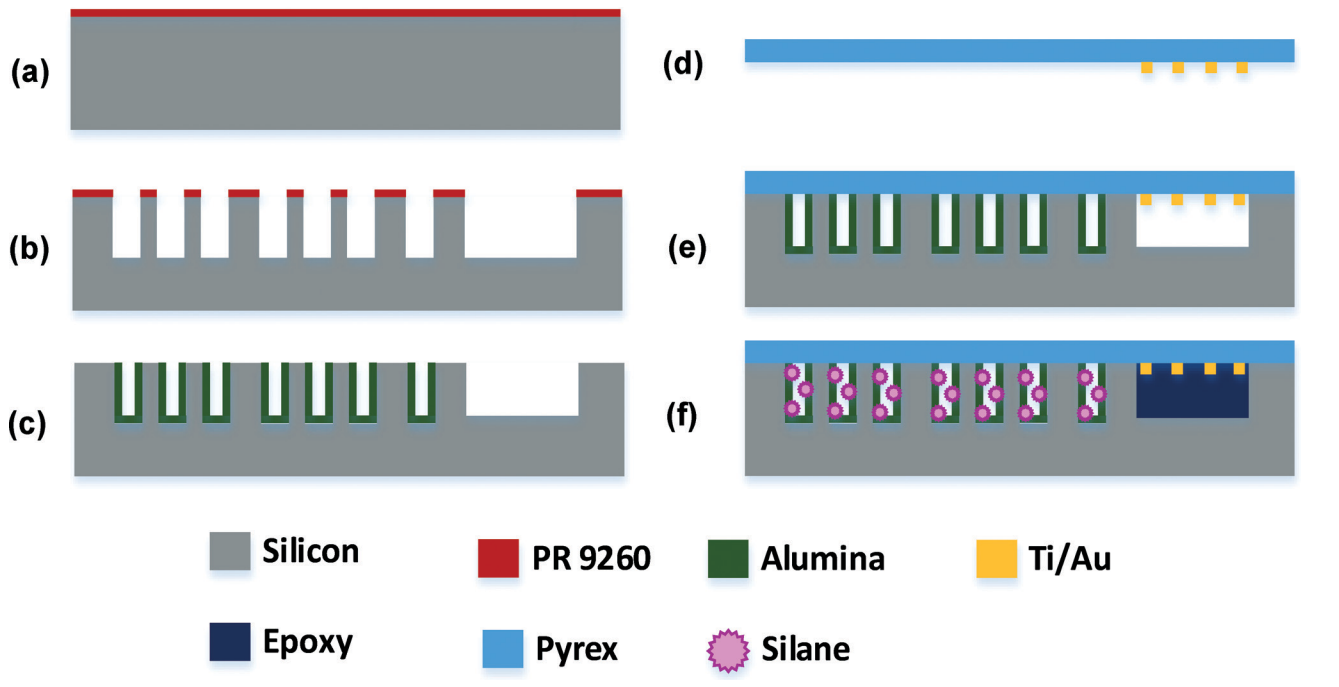

Fig. 2 Standard MEMS processes for the fabrication of the integrated chip. (a) Photolithography, (b) deep reactive ion etching, (c) atomic layer deposition, (d) physical vapor deposition, (e) anodic bonding and (f) surface functionalization.

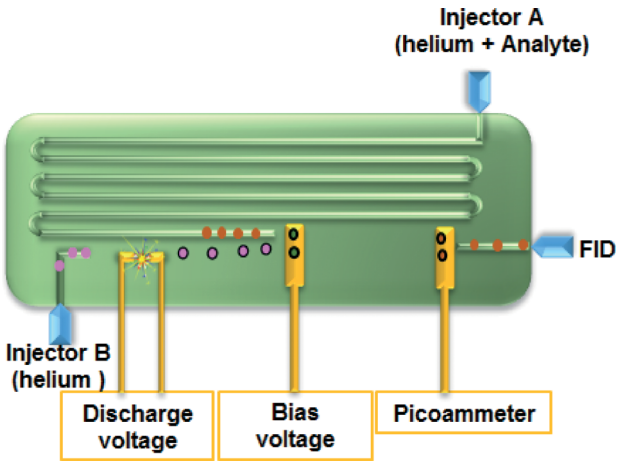

Fig. 3 Testing setup of the integrated chip inside the HP7890 benchtop GC system.

excessive amount of current flow which could damage the electrodes. A DC voltage was also applied to the bias electrode while a LABVIEW program recorded the measurement from the rear-terminal output using a Keithley 2700 multimeter.

Results and discussion

The optical images of the semi-packed μSC and the μDPID are shown in Fig. 4a and b, respectively. Fig. 4C shows the photograph of the entire chip with the external capillaries attached and the electrical connections affixed to the bond-pads. The inset shows the close-up of the micro-plasma across the 20 μm gap. Here we discuss the results of characterizing the μDPID first and then demonstrate the chromatographic analysis performed with the GC-on-chip.

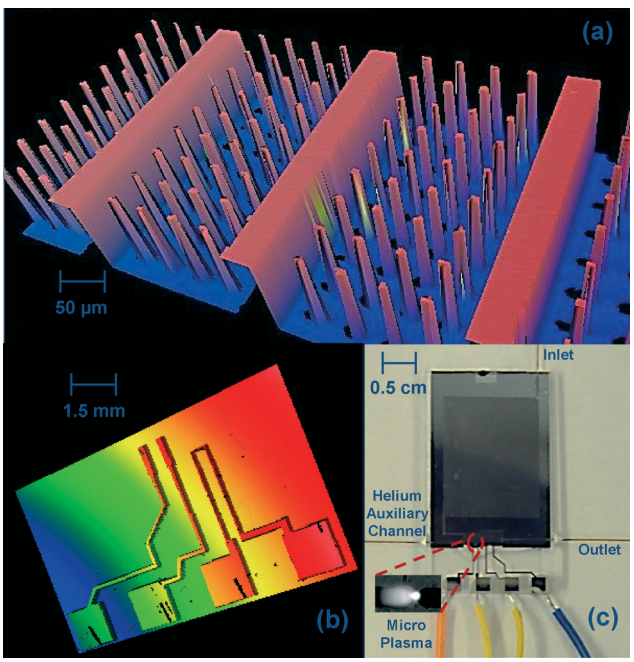

Fig. 4 Optical images of the actual fabricated devices. (a) μSC with the embedded pillars to serve as the separation stage, (b) metal electrodes on the Borofloat to serve as the detection stage and (c) complete chip after packaging.

Performance evaluation of the μDPID

Plasma characteristics. The circuit used for studying the electrical characteristics of the plasma is shown in the inset in Fig. 5. A 100 MΩ resistor and a 3.3 MΩ resistor were connected in series with the excitation electrodes of the packaged device. A helium flow rate of 1 mL min^{-1} was maintained through the device. The current through the plasma was calculated by measuring the voltage across the 3.3 MΩ resistor using a Keithley 2700 DMM. Fig. 5 shows the current–voltage plot of the plasma. For the discharge voltage less than 480 V, the current measured was on the order of tens of nanoamperes. At 500 V an unstable plasma was observed with the current changing anywhere between tens of nanoamperes and a few microamperes. A stable plasma was initiated when the discharge voltage was raised to 550 V with the current value measured around 2.5 μA. After 550 V, the plasma current was observed to increase linearly with the discharge voltage. The discharge voltage of 550 V was selected due to two reasons: 1) the photon energy from the plasma generated at 550 V was sufficient to ionize the compounds eluting from the μSC and 2) the operation of the detector under the stable plasma can be ensured with minimum power consumption. The power consumption at 550 V was determined to be 1.4 mW.

Mass flow rate sensitivity of the detector. In addition, the classification of μDPID as a mass flow rate sensitive detector (MSD) was demonstrated. The detectors typically employed for μGC can be categorized as either a concentration sensitive detector (CSD) or an MSD. The CSD measures the concentration of the compound in the carrier gas compared to the MSD which measures the absolute amount of the compound regardless of the volume of the carrier gas. The effect of the flow rate on the peak parameters for the same amount of

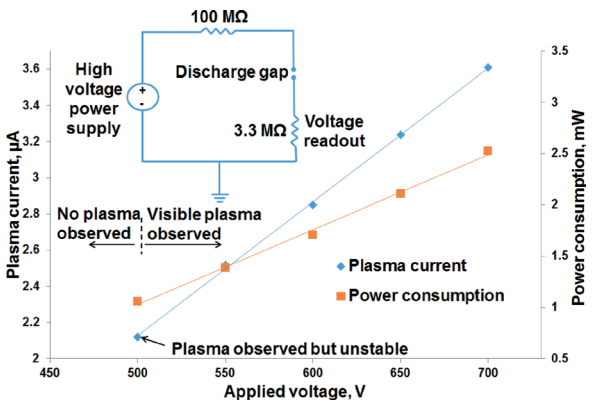

Fig. 5 Graph showing the current through the micro-plasma and power consumption of the μDPID as a function of the applied voltage. The electrical circuit used for measurement is shown in the inset.

sample can be used to distinguish between the two types of detectors.[32] For CSD with an increasing flow rate, the peak area decreases and the height is unchanged, whereas for the MSD the peak height is increased and the area is unchanged. The classification of μDPID as either CSD or MSD was determined by injecting the same amount of *n*-octane under different flow rates (by maintaining a constant split ratio of 100 : 1) and measuring effect on the peak properties of the compound. For that purpose, five runs were performed with injector A pressure set to the discrete values of 10, 12, 15, 20 and 25 psi. The pressure at the auxiliary channel was kept constant at 10 psi for each injection. The flow rate measured at the chip outlet corresponding to each pressure value was 0.9, 1.1, 1.4, 1.9 and 2.5 mL min^{-1}, respectively. Triplicate runs were performed for each value and the standard deviation was calculated. A 2 μl headspace volume of *n*-octane contained in a vial was sampled using an autosampler module to ensure repeatable injections. The peak width, height and area of the detector response was calculated and plotted as shown in Fig. 6. The graph shows that by increasing the flow rate the peak width decreases. It is important to recognize that the increased pressure (flow rate) forces the molecules to exit the volume of the detector cell faster resulting in a narrower peak width. However, the peak area remained unchanged (~160 pA s) which is reflected by the increase in the peak height. Similar relationship between the peak width and the height *vs.* the inlet pressure has been reported for FID.[32] These results signify that the μDPID measures the absolute mass of the compound and is therefore classified as a mass flow rate sensitive detector. Furthermore, the rise and fall times of the μDPID response were calculated. It is an important parameter which indicates the speed with which the detector can respond to the instantaneous changes of the input signal. Increasingly longer rise or fall time can vary the retention time of the compound, distort its peak shapes, and result in a wider peak width affecting the chromatographic resolution. The rise and fall times of the μDPID response for *n*-octane calculated at the flow rates of 0.9 and 2.5 mL min^{-1} were remarkably short. For 0.9 mL min^{-1} the rise time was

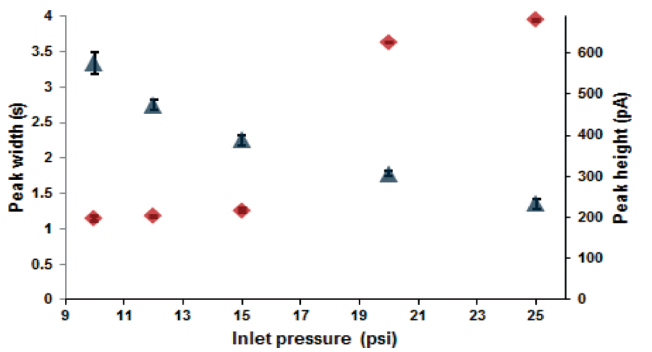

Fig. 6 Graph showing the effect of the flow rate on the peak shape (width and height) for a 2 μL headspace volume injection of *n*-octane. The triangle represents the peak width, whereas the diamond corresponds to the peak height. The peak area remained constant confirming the mass flow rate sensitivity of the μDPID.

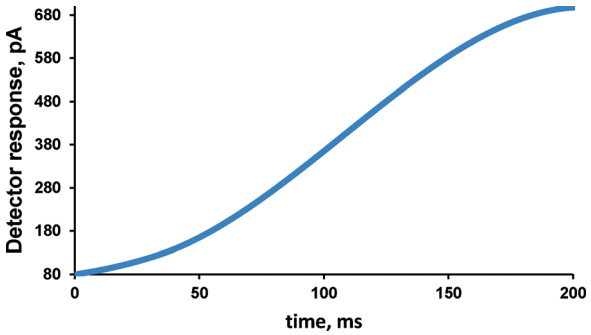

Fig. 7 Graph showing the rise time of the μDPID response for a 2 μL headspace volume of *n*-octane. The time required to rise from the baseline current of 80 pA to a peak value of 680 pA was ~200 ms.

~370 ms and the fall time was ~3 s, whereas for 2.5 mL min^{-1} these were noted to be ~200 ms (Fig. 7) and 1 s, respectively. Both these values indicate that the μDPID can respond effectively to the rapid changes of the input signal (~1 s wide peak).

Reliability assessment of the detector. The reliability of μDPID was investigated by examining the influence of its continuous operation on the response of the detector. The detector was challenged with a 2 μl headspace volume of *n*-octane with the pressure maintained at 10 psi at the inlet and auxiliary channel of the device. The flow rate measured at the outlet was 0.9 mL min^{-1}. The mean and the standard

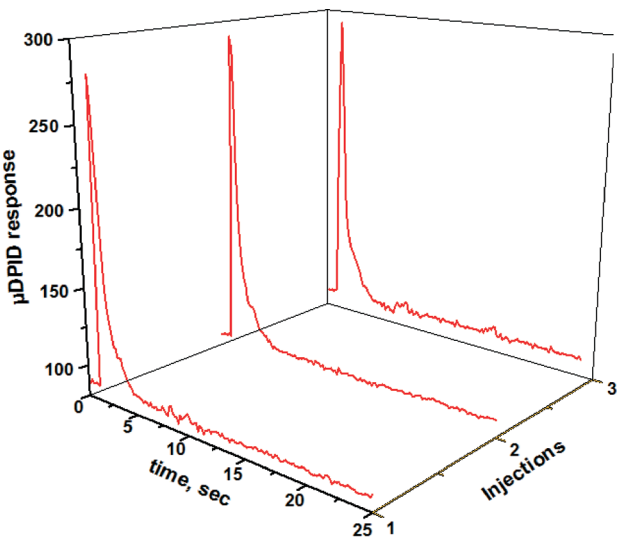

	Mean	Standard Deviation
Peak Height (pA)	199.3	8.22
Peak Width (s)	3.2	0.22
Peak Area (pA.s)	153.2	8.43

Fig. 8 Chromatogram showing the repeatability of the μDPID response for three injections performed every hour. The table shows the means and standard deviations of the peak parameters (height, width and area) for the injections of *n*-octane performed every hour over a continuous operation of 12 hours.

deviation of the peak area, width and height were calculated for the injections performed every hour over a time span of 12 hours. The experimental findings shown in Fig. 8 indicate that the μDPID produces highly repeatable results with less than 10% variations in the response. Moreover, no deterioration of the excitation electrodes was observed after the continuous operation for 12 hours.

Effect of bias voltage. The effect of bias voltage on the response of the detector was also examined. The bias voltage was increased from 0 to 60 V in increments of 10 V. The detector response was measured for a 7 μl headspace volume of *n*-octane injected with a split ratio of 100 : 1. The pressures at injectors A and B were maintained at 15 psi and 10 psi, respectively. Fig. 9 shows the effect of the bias electrode voltage on the detector response. Initially, ~10 pA increase in the *n*-octane peak height was observed for every 10 V rise in the bias voltage. This is attributed to the fact that by increasing the bias voltage, the negatively charged species from the ionizing flux are collected more effectively at the bias electrode. This reduces the probability of their recombination inside the collector volume with the positive ions produced by the ionization of the compound. The recombination process can cause a portion of the generated ions to be neutralized and hence not detected. Thus, by increasing the bias voltage, an increase in the collector current is observed. However, beyond 30 V, the bias voltage is strong enough to repel the positively charged species in the ionizing flux; as a result a decrease in the detector response with increasing the bias voltage beyond 30 V is observed.

Limit of detection. Generally, the smallest signal that can be safely attributed to the compound is the one with a signal to noise ratio (S/N) of three or more. Therefore, S/N = 3 was specified as the criteria for measuring the limit of detection (LOD) for a particular compound in the characterization of the μDPID. LOD for *n*-octane was evaluated by operating the integrated chip under isothermal conditions at 40 °C with the pressures at injectors A and B set to 15 psi and 10 psi, respectively. 0.5, 1 and 1.5 μL volumes of the 5 ppm *n*-octane sample prepared as explained in the Materials section were injected into the chip. The split ratio was maintained at 150 : 1 and the bias voltage was set to 0 V during the analysis. These volumes translate to ~10, 20 and 30 pg of *n*-octane, respectively.[18] The response profiles from the μDPID for these three injected mass of *n*-octane with the corresponding FID results are shown in Fig. 10. The retention time for *n*-octane was around 0.35 min. A 10-point moving average filter was used to make the high-frequency noise smooth. The S/N values for these three injections were calculated to be 3.6, 16 and 22, respectively, for the μDPID. These results clearly indicate that the LOD as low as ~10 pg is possible with the μDPID. The corresponding S/N values for the FID were found to be 3, 8 and 10, respectively. Afterwards, the bias voltage was varied to improve the *n*-octane peak signal. Table 2 shows that the peak height of *n*-octane was doubled by increasing the bias voltage to 30 V signifying opportunity for further improvement in the LOD. It should be noted that the LOD depends upon the testing compound properties in addition to the system operating conditions. For instance, the compound may experience significant band broadening due to the presence of extra-column volume or with increasing retention time which could result in wider peaks and higher LOD. Similarly, the temperature and flow rate play an important role in increasing the peak height especially for the late eluting compounds which can create significant impact on the LOD.

Performance evaluation of the GC-on-chip

Following the performance evaluation of the μDPID, the monolithic integrated chip was tested. It should be noted that ALD-treated/silane-functionalized semi-packed μSCs have yielded ~4200 plates per meter, using *n*-decane at 50 °C at the inlet pressure of 7.5 psi (linear velocity, 8.5 cm s^{-1}) as recently demonstrated by our group.[11] The chromatographic performance of individual μSCs, however, was tested in our previous work only under isothermal conditions.[11] The presented work herein evaluates the separation efficiency of the column under simultaneous flow and temperature programming while using the on-chip detection stage. The GC-on-chip performance was evaluated with an eight-compound mixture containing alkanes and aromatic hydrocarbons

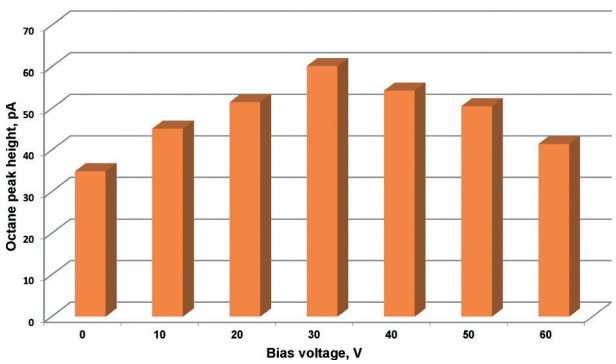

Fig. 9 Response of the μDPID for a 7 μL headspace volume of *n*-octane *versus* bias voltage. Each data point is the average of three replicates.

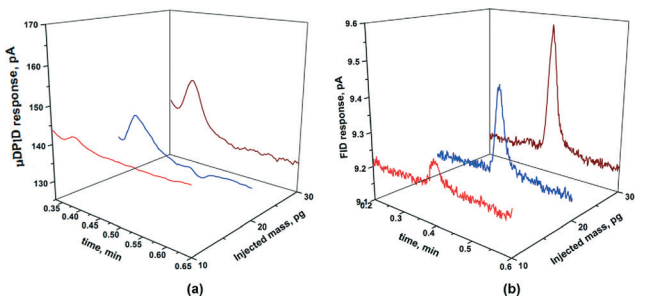

Fig. 10 (a) Response profiles from the μDPID for ~10, 20 and 30 pg injection of *n*-octane. A 10-point moving average filter was used to make the high-frequency noise smooth. (b) Response from the FID for the corresponding injections.

Table 2 The effect of bias voltage on the peak height of *n*-octane for ~10 pg injection. The signal to noise ratio (S/N) was doubled by increasing the bias voltage to 30 V

Bias voltage, V	Peak height, pA	S/N
0	1.8	3.6
10	3	6
20	3.1	6.2
30	3	6

prepared as explained before. The chip was configured inside an HP7890 GC system as shown in Fig. 3. Injectors A and B were set to 15 psi and 10 psi, respectively. A 550 V DC voltage was applied to create the discharge and the bias voltage was set to 20 V. The chip was maintained under isothermal conditions at 40 °C. The resulting chromatographic separation was achieved in 2.5 min (Fig. 11a), providing good resolution and retention of the compounds. The tested compounds were eluted in the order of increasing boiling points with the most volatile compound eluting first. The air peak (not shown here) precedes the *n*-heptane compound which shows the universality of the μDPID. A similar response was observed on the FID (Fig. 11b) except for the air peak which could not be detected due to the selectivity of the detector to only organic compounds. As seen in the chromatogram, the first six compounds were baseline separated from each other; however, *p*-xylene, C_9 and C_{10} peaks were separated well from each other resulting in an increased analysis time. The resolution (R_s) is defined as

$$R_s = \frac{(t_r)_B - (t_r)_A}{\frac{(w_b)_A + (w_b)_B}{2}} = \frac{2d}{(w_b)_A + (w_b)_B} \quad (1)$$

where d is the distance between the peak maxima for the two compounds, A and B; w_b is the peak width at the base. The resolutions were noted to be 5 between *p*-xylene and C_9 and 18.6 between C_9 and C_{10}, while their peak width values were noted to be 4.2, 3 and 7 s, respectively. Raising the temperature of the chip or increasing the flow rate was considered to reduce the analysis time. However, it resulted in poor resolution among the early eluting peak. Therefore, flow and temperature programming techniques were utilized in these ALD-coated μSCs for the first time to accelerate the separation of *p*-xylene, C_9 and C_{10} with an effort to achieve satisfying resolution between all the other compounds. This was achieved by first flow programming the μSC while maintaining the chip under isothermal conditions at 40 °C. The injector A pressure was initially maintained at 15 psi (1.3 mL min^{-1}) for 0.7 min (holdup time) and then increased to 35 psi (2.7 mL min^{-1}) at a rate of 30 psi min^{-1}. The hold time of 0.7 min was necessary to achieve baseline separation between the first six eluting compounds. Reducing the holdup time causes early eluting peaks to merge together degrading the overall separation resolution. The chromatogram in Fig. 12 reveals that the separation was completed in 1.8 min (28% reduction in the analysis time) with resolutions of 5.8 between *p*-xylene and C_9 and 15 between C_9 and C_{10}. It should be noted from the chromatogram that the peak width of C_9 was reduced to 2.9 s (3% reduction) while that of C_{10} was reduced to 4.5 s (35% reduction). The peak heights of *p*-xylene, C_9 and C_{10} also increased due to the increased flow rate during the flow programmed run providing better detection of the late eluting compounds. Another effective method for reducing the analysis time is the temperature programming of the μSC. In this process, the μSC temperature increases which decreases the partition coefficient of the compounds still inside the column so they can move faster yielding a decrease in the retention time. As explained before, temperature programming ($T_{initial}$ = 40 °C, ramp = 30 °C min^{-1}, T_{final} = 65 °C) in conjunction with flow programming of the chip shortened the analysis time considerably. Fig. 13 indicates that the complete separation was achieved in 0.8 min (68% reduction in the analysis time) while the peak width values of *p*-xylene, C_9 and C_{10} were noted to be ~1.8, 2.1 and 3 s, respectively. As expected, a further decrease in the resolution was also observed. These findings have been compiled and presented in Table 3. To further shorten the analysis time for high-boiling hydrocarbons, a series of

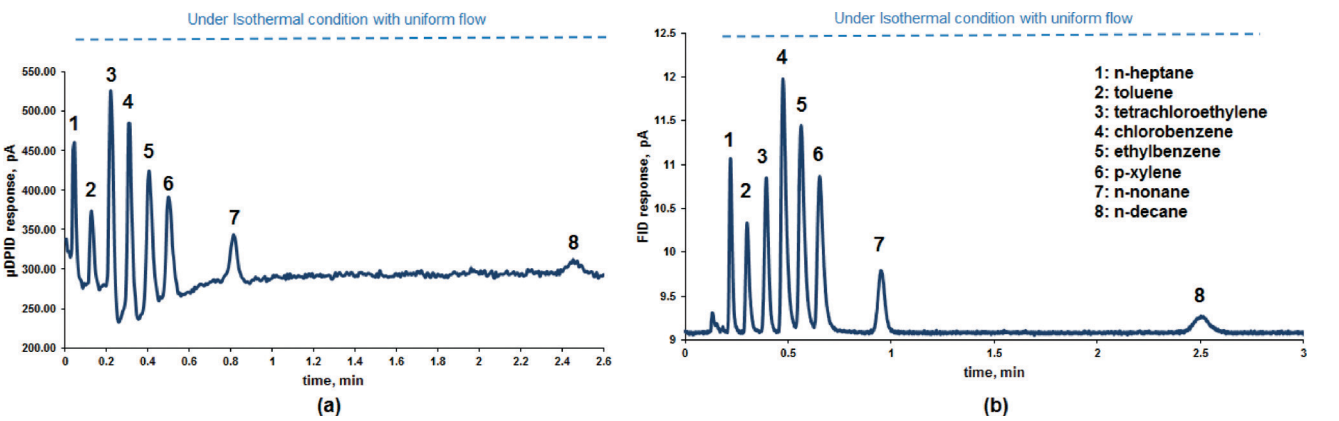

Fig. 11 (a) Response of the μDPID to a 10 μL headspace volume of an eight-compound mixture under isothermal conditions at 40 °C and a flow rate of 1.33 mL min^{-1}. (b) Corresponding chromatogram generated by the FID.

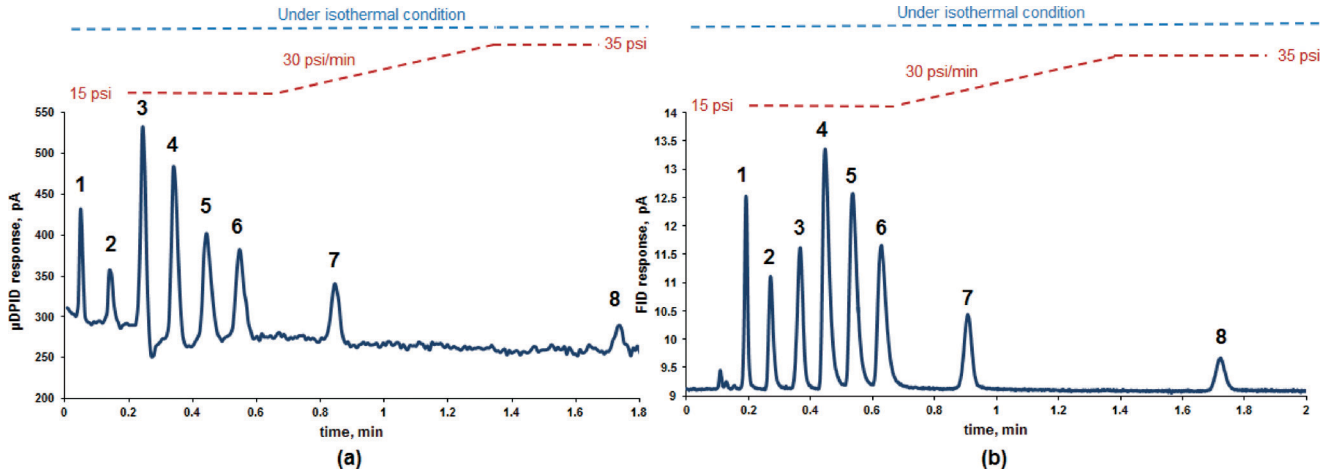

Fig. 12 (a) Response of the μDPID to a 10 μL headspace volume of an eight-compound mixture under the flow programming and isothermal conditions at 40 °C. The initial and final flow rates through the column were 1.3 mL min^{-1} and 2.7 mL min^{-1}, respectively. (b) Corresponding chromatogram generated by the FID.

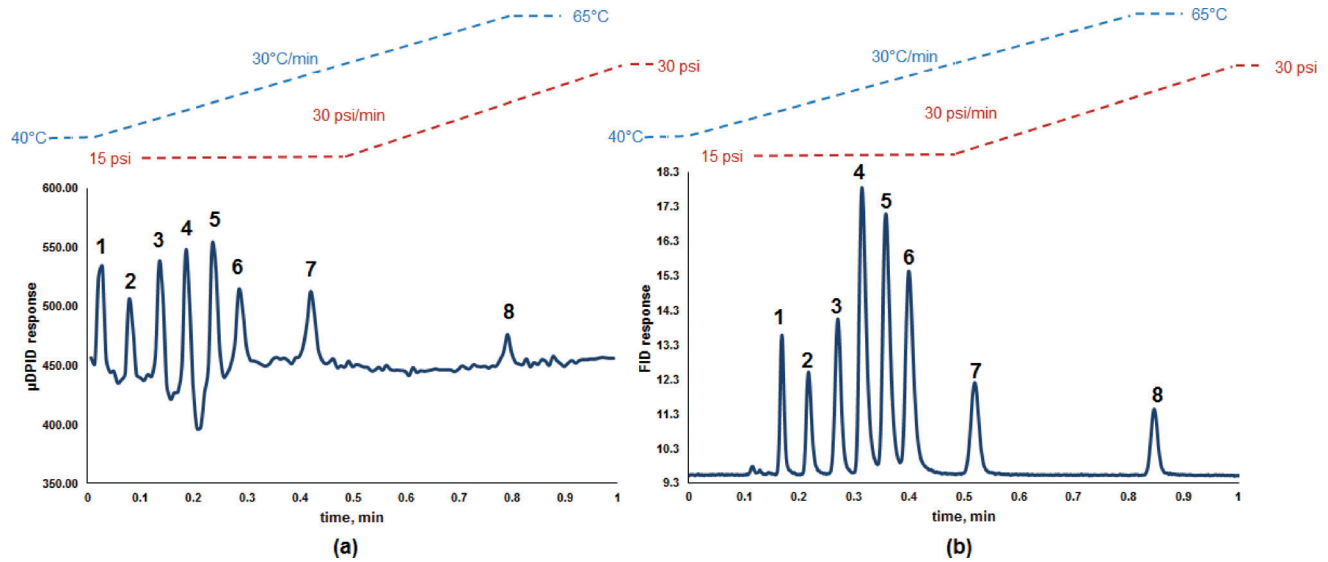

Fig. 13 (a) Response of the μDPID to a 10 μL headspace volume of an eight-compound mixture under the flow and temperature programming conditions. The initial and final flow rates through the column were 1.3 mL min^{-1} and 2.3 mL min^{-1}, respectively. (b) Corresponding chromatogram generated by the FID.

Table 3 Summary of the results from Fig. 11 to 13 for the late eluting compounds including *p*-xylene, *n*-nonane and *n*-decane. The results are summarized in terms of the peak width, the retention time and the resolution

	p-Xylene		*n*-Nonane (C_9)		*n*-Decane (C_{10})		Resolution $\frac{(t_r)_B-(t_r)_A}{\frac{(w_b)_A+(w_b)_B}{2}}$	
Testing conditions	Retention time (s)	Peak width (s)	Retention time (s)	Peak width (s)	Retention time (s)	Peak width (s)	*p*-Xylene–C_9	C_9–C_{10}
Isothermal, 40 °C	30	4.2	48	3	141	7	5	186
Flow programmed run	30	3.3	48	2.9	104	4.5	5.8	15
Flow and temperature programmed run	17	1.8	25	2.1	47	3	4.3	8.4

exploratory trials were performed with four *n*-alkanes (C_9–C_{12}) to establish the flow and temperature conditions for the best possible separation in the shortest period. For that purpose, the chip temperature was raised to 100 °C with the injector A pressure maintained at 25 psi (1.9 mL min^{-1}). A 50 μL headspace volume of a four-compound mixture prepared as explained in the Materials section was injected into the chip. The resulting chromatogram (Fig. 14) shows the separation and detection of these compounds in less than a minute. The peak width values were 1.3, 1.7, 3 and 5.4 s for C_9, C_{10}, C_{11} and C_{12}, respectively. It can be deduced from the results shown in Fig. 11–14 that faster analysis of complex samples with compounds, covering a wide range of boiling point, is possible through the optimization of flow rate and temperature settings of the chip. A baseline signal with <5 pA of the noise level in these chromatograms clearly demonstrates the simultaneous temperature and flow programming capabilities of our newly developed GC-on-chip module. Such a stable response was not possible in our previously published work when the monolithically integrated chip with μTCD was subjected to temperature and flow programming conditions. However, small dips (negative peaks) in the baseline signal in the chromatograms (Fig. 11a–13a) were observed between few compounds which might be related to the time response of the detector. The exact origin of these dips is unclear at this stage and will be ascertained in future investigations. It is important to note that such variations in the response have been observed with the chemiresistor (CR) sensors as well.[32] Furthermore, these results (Fig. 11a–14a) present a proof-of-principle that rapid chromatographic analysis of a mixture containing low- and high-boiling point compounds can be achieved through multiple GC-on-chip modules operated in parallel under different temperature and flow rate conditions.

Conclusions

The μDPID presented in this article has many desired features that bode well for its use in μGC. The detector is easy to fabricate and requires silicon and glass substrates which are the most commonly used materials for fabrication of μGC components. This provides the opportunity of its monolithic integration with other μGC modules such as the μSC reported in this article. This integration reduces the disadvantages of hybrid arrangement of μGC components including the dead-volume along the flow path, the overall size and the implementation cost. Furthermore, the detector resistance to temperature and flow rate variations allows the programming of the μSC to achieve faster analysis with better performance. We have demonstrated that through temperature and flow programmed operation of the μSC, 68% reduction in the analysis time compared to the isothermal conditions can be achieved. Similarly, operating the chip under an elevated temperature with a higher carrier gas flow rate can provide quick separation and detection of high boilers. Furthermore, a network of these chips working in parallel can be envisioned with each row maintained under different temperature and carrier gas flow rate conditions to enable the rapid separation of low- and high-boiling point compounds. Rapid response time of the μDPID enables the detection of sharp peaks (~1 s wide) which can be beneficial in high speed μGCs. The LOD (~10 pg) attained with the μDPID is significantly lower than other detectors typically used within the μGC community.[26,32,33] Additionally, the fact that the bias voltage can increase the signal level provides excellent opportunity to improve the LOD which can be realized through the modifications in the design and location of the bias electrode. In the future, we will study the influence of the distance between the discharge and the outlet of the μSC and the size of the collector volume on the detector performance. We are pursuing these design alterations along with the electronic board development for the μDPID. The circuit board will generate the high voltage (550 V, 2.5 μA) required for plasma generation. It will also provide the necessary current limiting protection circuitry to eliminate the possibility of electrical hazards as well as the interface for processing the pico-ampere level of the current signal for μDPID.

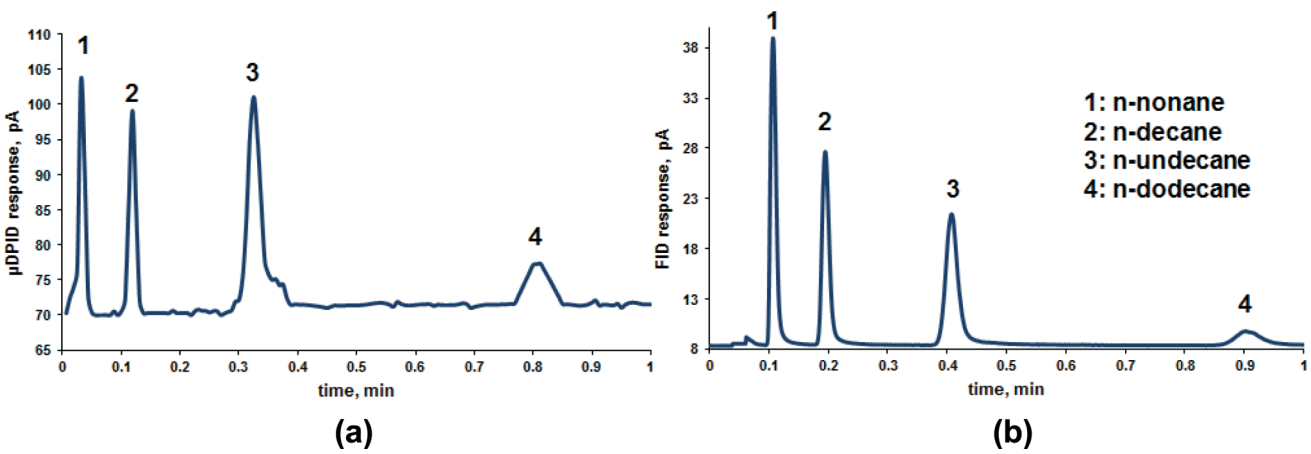

Fig. 14 (a) Response of the μDPID to a 50 μL headspace volume of a four-compound mixture of high boilers under isothermal conditions at 100 °C and a flow rate of 1.9 mL min^{-1}. (b) Corresponding chromatogram generated by the FID.

Acknowledgements

The authors would like to thank Mr. Donald Leber with the MicrOn Cleanroom at Virginia Tech. This work was supported by the National Institute for Occupational Safety and Health (NIOSH) under award no. 1R21OH010330 and the National Science Foundation (NSF) under award no. ECCS-1002279.

Notes and references

1 F. L. Dorman, J. J. Whiting, J. W. Cochran and J. Gardea-Torresdey, *Anal. Chem.*, 2010, **82**, 4775–4785.
2 A. Boots, A. Smolinska, J. van Berkel, R. Fijten, E. Stobberingh, M. Boumans, E. Moonen, E. Wouters, J. Dallinga and F. Van Schooten, *J. Breath Res.*, 2014, **8**, 027106.
3 A. Wilson, *J. Forensic Sci. Criminol.*, 2014, **1**, S103.
4 S. Giannoukos, B. Brkić, S. Taylor and N. France, *J. Am. Soc. Mass Spectrom.*, 2014, 1–9.
5 M. Akbar and M. Agah, *J. Microelectromech. Syst.*, 2013, **22**, 443–451.
6 M. Akbar, D. Wang, R. Goodman, A. Hoover, G. Rice, J. R. Heflin and M. Agah, *J. Chromatogr. A*, 2013, **1322**, 1–7.
7 Y. Mohsen, J.-B. Sanchez, F. Berger, H. Lahlou, I. Bezverkhyy, V. Fierro, G. Weber, A. Celzard and J.-P. Bellat, *Sens. Actuators, B*, 2013, **176**, 124–131.
8 Y.-S. Lin, C.-Y. Kuo, W.-C. Tian, T.-H. Wu, H.-J. Sheen, H.-Y. Kuo and C.-J. Lu, *Batch fabrication of micro preconcentrator with thin film microheater using Tollen's reaction*, 2013.
9 R. Haudebourg, J. Vial, D. Thiebaut, K. Danaie, J. Breviere, P. Sassiat, I. Azzouz and B. Bourlon, *Anal. Chem.*, 2012, **85**, 114–120.
10 M. Agah and K. D. Wise, *J. Microelectromech. Syst.*, 2007, **16**, 853–860.
11 H. Shakeel, G. W. Rice and M. Agah, *Sens. Actuators, B*, 2014, **203**, 641–646.
12 H. Shakeel, D. Wang, R. Heflin and M. Agah, *IEEE Sens. J.*, 2014, **14**, 3352–3357.
13 B.-X. Chen, T.-Y. Hung, R.-S. Jian and C.-J. Lu, *Lab Chip*, 2013, **13**, 1333–1341.
14 J. Sun, D. Cui, X. Chen, L. Zhang, H. Cai and H. Li, *J. Chromatogr. A*, 2013, **1291**, 122–128.
15 A. Wang, S. Hynynen, A. R. Hawkins, S. E. Tolley, H. D. Tolley and M. L. Lee, *J. Chromatogr. A*, 2014, **1374**, 216–223.
16 S. Zimmermann, P. Krippner, A. Vogel and J. Müller, *Sens. Actuators, B*, 2002, **83**, 285–289.
17 E. Covington, F. Bohrer, C. Xu, E. Zellers and C. Kurdak, *Lab Chip*, 2010, **10**, 3058–3060.
18 S. Narayanan, G. Rice and M. Agah, *Microchim. Acta*, 2014, **181**, 493–499.
19 S. C. Terry, J. H. Jerman and J. B. Angell, *IEEE Trans. Electron Devices*, 1979, **26**, 1880–1886.
20 W. R. Collin, G. Serrano, L. K. Wright, H. Chang, N. Nuñovero and E. T. Zellers, *Anal. Chem.*, 2013, **86**, 655–663.
21 S. Zampolli, I. Elmi, F. Mancarella, P. Betti, E. Dalcanale, G. Cardinali and M. Severi, *Sens. Actuators, B*, 2009, **141**, 322–328.
22 M. Akbar, S. Narayanan, M. Restaino and M. Agah, *Analyst*, 2014, **139**, 3384–3392.
23 Y. Mohsen, H. Lahlou, J.-B. Sanchez, F. Berger, I. Bezverkhyy, G. Weber and J.-P. Bellat, *Microchem. J.*, 2014, **114**, 48–52.
24 C. Chen, F. Tsow, K. D. Campbell, R. Iglesias, E. Forzani and N. Tao, *IEEE Sens. J.*, 2013, **13**, 1748.
25 A. Garg, M. Akbar, E. Vejerano, S. Narayanan, L. Nazhandali, L. C. Marr and M. Agah, *Sens. Actuators, B*, 2015, DOI: 10.1016/j.snb.2014.12.136.
26 B. C. Kaanta, H. Chen and X. Zhang, *J. Micromech. Microeng.*, 2010, **20**, 055016.
27 S. Narayanan and M. Agah, *J. Microelectromech. Syst.*, 2013, **22**, 1166–1173.
28 S. Narayanan, B. Alfeeli and M. Agah, *IEEE Sens. J.*, 2012, **12**, 1893–1900.
29 K. Reddy, Y. Guo, J. Liu, W. Lee, M. K. K. Oo and X. Fan, *Lab Chip*, 2012, **12**, 901–905.
30 Y. Sun, J. Liu, D. J. Howard, G. Frye-Mason, A. K. Thompson, S.-J. Ja and X. Fan, *Analyst*, 2010, **135**, 165–171.
31 S. Narayanan, G. Rice and M. Agah, *Sens. Actuators, B*, 2015, **206**, 190–197.
32 Q. Zhong, W. H. Steinecker and E. T. Zellers, *Analyst*, 2009, **134**, 283–293.
33 K. Scholten, X. Fan and E. T. Zellers, *Lab Chip*, 2014, **14**, 3873–3880.

